Acoustics Australia
https://doi.org/10.1007/s40857-024-00332-0

ORIGINAL PAPER

Numerical Investigation on Aerodynamic Noise Source Identification and Far-Field Noise Characteristics of the High-Speed Train Bogie Region

Jiawei Shi[1] · Jiye Zhang[1] · Tian Li[1]

Received: 17 June 2024 / Accepted: 2 August 2024

Abstract
The bogie region is one of the most important aerodynamic noise sources of high-speed trains. A thorough understanding of the generation mechanism and characteristics of bogie aerodynamic noise is the prerequisite for effective implementation of noise control measures. In this study, a delayed detached eddy simulation (DDES) is performed to solve the unsteady flow field around the bogie region, and an aerodynamic noise source identification method based on the integral solution of the Ffowcs Williams-Hawkings (FW-H) equation is adopted to determine the dipole and quadrupole sources distribution in the bogie region. The identification results of the two types of sources provide different understandings of the noise generation mechanism of the bogie region but determine the same flow structures closely associated with the bogie aerodynamic noise, which are the shear vortex structures formed at the rear edge of the cowcatcher and the front side edges of the bogie cavity. The flow field data obtained by DDES simulation is also used as input for the FW-H solver to calculate far-field noise, and the source contribution, spectrum characteristics and directivity of the far-field noise are analyzed. The results show that at a speed of 350 km/h, the aerodynamic noise in the bogie region is still dominated by dipole sources, and the contributions of the bogie itself and the bogie cavity to far-field noise are equally important despite the significant differences in their radiation characteristics.

Keywords Bogie · Cavity · Aerodynamic noise · Noise source identification · Far-field noise

1 Introduction

Noise pollution is one of the main impacts of high-speed train operation on the surrounding environment. It is generally believed that when the train speed exceeds 300 km/h, aerodynamic noise will gradually exceed rolling noise and occupy a dominant position [1]. Nowadays, train operation speeds have achieved 300 km/h in many countries, and people are still making efforts for further improvements. To meet the requirements of increasingly stringent environment protection regulations and ensure the sustainable development of high-speed railways, aerodynamic noise control has become an important consideration during the design of high-speed trains [1, 2]. A thorough understanding of the generation mechanism and characteristics of the train aerodynamic noise is the prerequisite for effective noise control.

During high-speed train operation, violent flow separation and turbulence mixing occur at the unsmooth areas of the train body. These areas are also the main aerodynamic noise sources of the train, usually including the bogie region, pantograph region, inter-coach spacing, etc. [1, 2]. Compared with other aerodynamic noise sources, the aerodynamic noise generated in the bogie region is more complex. The bogie is mechanically complex, the traction, guidance and braking functions are all realized by it, and it also needs to bear the weight of the carbody and cushion the impact caused by the track irregularity. As a key component that determines the driving safety and running quality of the train, its design is mainly constrained by requirements of dynamic performance, structural strength, and maintenance convenience rather than aerodynamic and aeroacoustics performance. This causes a large number of components clustered together in a highly nonaerodynamic shape, making the turbulence in the bogie region highly dense and flow pattern complex.

✉ Jiye Zhang
jyzhang@swjtu.edu.cn

[1] State Key Laboratory of Rail Transit Vehicle System, Southwest Jiaotong University, Chengdu 610031, China

Published online: 14 August 2024

Besides, the flow field in the bogie region is also affected by ground effects, wheel rotation and carbody structures [3–6].

Same as other aerodynamic noise issues, research on aerodynamic noise of the bogie region mainly relies on experiment and numerical simulation. In terms of experimental research, He et al. [7] used an array with 78 microphones to measure the external noise of a high-speed train running at 390 km/h. The results show that the train external noise is mainly generated from the bogie region, especially the first bogie of the leading car. Yamazaki et al. [8] tested the underbody flow of a train and found that for the ground-fixed coordinate system, the flow velocity increases sharply from the train nose to the second car and then becomes almost constant, which means that for the coordinate system moving with the train, the first bogie of the leading car has the highest inflow velocity. This was considered to be the reason that the aerodynamic noise generated by the first bogie of the leading car is much higher than that generated by other bogies. Since, the noise signals measured in line tests contain both rolling noise and aerodynamic noise, and there is no widely recognized method to separate them, it is difficult to determine their respective contributions and characteristics.

Compared with the line test, the wind tunnel test provides a more controllable environment, enabling separate investigation of the bogie aerodynamic noise. Lauterbach et al. [9] conducted wind tunnel tests on a 1:25 scale ICE3 train model. The results show that the aerodynamic noise of the bogie region is concentrated in the frequency band below 5000 Hz and can be characterized by cavity noise model. Hao [10] analyzed the wind tunnel test results of aerodynamic noise generated by 1:8 scale three-car models with different configurations. He also found that the noise energy of the bogie region is mainly concentrated in mid and low frequency bands, but his test results exhibit as broadband noise in whole frequency band with no obvious peak in the spectra. Iglesias et al. [11] tested the aerodynamic noise of 1:7 scale bogie models in anechoic wind tunnel and found that the components exposed to free flow are main noise sources. Yamazaki et al. [12] conducted wind tunnel test on a 1:7 scale bogie model and analyzed the contribution of each component to total noise by gradually removing the components of the bogie model. The test results indicate that the wheels exposed to the outer flow are important noise sources, while the motor and brake that located inside the bogie cavity also make certain contributions. Sawamura et al. [13] conducted wind tunnel tests to identify the aerodynamic sound source of a 1:7 scale bogie model using a 2-D microphone array positioned beneath the bogie model. They found that strong sound sources appear in the rear section of the bogie region. Specifically, the noise at around 250–315 Hz is generated by the cavity structure and the noise sources at around 400–500 Hz appear on the surfaces of the traction motors and gear units.

Although the existing experimental studies have presented many aeroacoustics phenomena related to the bogie region, the limited flow field data obtained from the tests cannot fully reveal the underlying mechanism. Compared with the experimental research, the numerical simulation can obtain more abundant flow field information, and a detailed CFD analysis is helpful to provide a profound insight into the generation mechanism of aerodynamic noise. Meskine et al. [14] combined the lattice Boltzmann method (LBM) and FW-H equation to numerically simulate the aerodynamic noise of a full-scale simplified train model and provided the full-spectrum noise results of pantographs, bogies, and intercoach gaps. The acoustic energy of these aerodynamic noise sources is concentrated in the frequency band below 2000 Hz, and the first bogie of the leading car is the main noise contributor in the frequency band below 150 Hz. Sun et al. [15] investigated the near-field noise characteristics of the bogie region using a nonlinear acoustics solver (NLAS). The results indicate that the near-field noise in the downstream area of the first bogie of the head car was slightly higher than that in the upstream area. Zhu et al. [4, 16, and 17] numerically analyzed the unsteady flow field and aerodynamic noise characteristics of a very simplified bogie model. As the model in his studies only includes wheelsets and simple side frames, the results may not be applicable to real bogie models. Minelli et al. [18] numerically studied the aerodynamic and aeroacoustics characteristics of a 1:25 scale head car of ICE3 train. They pointed out that the aerodynamic noise generated by the bogie cavity is closely related to two flow patterns, which are the jet at the bottom of the cowcatcher and the shear layer flow at the cavity side. However, due to that only the bogie cavity is modeled, the influences of the bogie on the cavity flow field and far-field noise remain unclear, the coupling effects between the cavity and bogie need to be further investigated. Li et al. [19] adopted subdomain method to simulate the flow field of a full-scale train head shape and performed contribution and coherence analyses. They pointed out that the frame, bogie cavity, and wheelsets have significant contributions to the bogie noise. In a recent study, He et al. [20] developed a hybrid grid system and applied it to bogie aerodynamic noise simulation. The simulation results show that the outer components of the bogie that are immersed in the turbulent wake from upstream experience strong pressure fluctuation, serving as main noise sources of the bogie.

Based on above review, the relationship between flow structures and aerodynamic noise of the bogie region remains to be further investigated, and the previous analysis on aerodynamic noise radiation characteristics of the bogie aerodynamic noise is not yet in-depth enough. In this paper, a CFD based aerodynamic noise source identification method is established to determine the distribution of dipole and quadrupole sources in the bogie region, and the generation

mechanism of the bogie aerodynamic noise is revealed combined with the flow field analysis from the perspective of aerodynamic noise sources. The source contribution, spectrum characteristics, as well as the directivity of the far-field noise of the bogie region are discussed in detail. These sound radiation characteristics are also explained by the distribution of aerodynamic sound sources. Compared with the previous studies, the current study provides a new perspective to understand the generation mechanism and radiation characteristics of the bogie aerodynamic noise, and the relevant results could provide targeted guidance for aerodynamic noise control of the high-speed train bogie region.

2 Numerical Methods

2.1 DDES Model

The detached eddy simulation (DES) is specifically designed for high Reynolds number wall bounded flow. In the DES model, the Reynolds average Navier–Stokes (RANS) model is employed in near wall region to avoid the huge computational cost of resolving boundary layer by using large eddy simulation (LES), and the LES treatment in separation region can capture the flow field fluctuations dominated by large-scale turbulent structures more accurately. Based on the original DES model, Menter and Kuntz [21] proposed the delayed detached eddy simulation (DDES) based on the shear stress transport (SST)$k-\omega$ model to solve the issue of grid induced separation. Shur et al. [22] proposed the improved delayed detached eddy simulation (IDDES) by combining the DDES model with wall modeled LES to address the issue of log-layer mismatch. In recent years, both the DDES and IDDES models have been widely used to calculate the unsteady flow field of high-speed trains. According to our previous test of the turbulence model [23, 24], the SST $k-\omega$ based DDES model is adopted to numerically solve the unsteady flow field in the bogie region in this work.

In the SST $k-\omega$ model, the governing equations of turbulent kinetic energy k and specific dissipation rate ω are [25]

$$\frac{\partial(\rho k)}{\partial t}+\nabla.(\rho k\overline{\mathbf{u}})=\nabla.[(\mu+\sigma_k\mu_t)\nabla k]+P_k-\rho\beta^* f_{\beta^*}(\omega k-\omega_0 k_0)+S_k \quad (1)$$

$$\frac{\partial(\rho\omega)}{\partial t}+\nabla.(\rho\omega\overline{\mathbf{u}})=\nabla.[(\mu+\sigma_\omega\mu_t)\nabla\omega]+P_\omega-\rho\beta f_\beta\left(\omega^2-\omega_0^2\right)+S_\omega \quad (2)$$

wherein, ρ is the fluid density, $\overline{\mathbf{u}}$ is the time-averaged flow velocity, t is the time, μ is the dynamic viscosity, σ_k,σ_ω,β^* and β are model coefficients, μ_t is the eddy viscosity coefficient, P_k and P_ω are production terms, f_{β^*} and f_β are the free-shear modification factor and the vortex-stretching modification factor, respectively; S_k and S_ω are source terms, k_0 and ω_0 are the ambient turbulence values for counteracting turbulence decay. For the SST $k-\omega$ based DDES model, the specific dissipation rate ω in Eq. (1) is replaced by $\tilde{\omega}=\omega\phi$, $\phi=\max(l_{\text{ratio}}F,\ 1)$, l_{ratio} is the ratio of the length scale of RANS model to that of LES model, $F=1-F_2$ is the switching function (F_2 is the boundary layer identification function in the original SST $k-\omega$ model and acts as a delay factor here). This modification delays the switch from RANS model to LES model in the boundary layer, reducing the dependence of the DES model on grids. More detailed information about the DDES model can be found in [21, 25].

2.2 FW-H Equation and Its Acoustic Analogy Integral Solution

The FW-H equation is the theoretical description of sound generated by the interaction between moving objects and fluids [26], as shown in Eq. (3),

$$\frac{1}{c_0^2}\frac{\partial^2}{\partial t^2}\left[p'\mathrm{H}(\mathrm{f})\right]-\nabla^2\left[p'\mathrm{H}(\mathrm{f})\right]=\frac{\partial}{\partial t}\left[\rho_0 \mathrm{v_n}\delta(\mathrm{f})\right]-\frac{\partial}{\partial x_i}\left[p_{ij}\hat{n}_j\delta(\mathrm{f})\right]+\frac{\partial^2}{\partial x_i\partial x_j}\left[T_{ij}\mathrm{H}(\mathrm{f})\right] \quad (3)$$

where c_0 is the speed of sound, t is the time, p' is the sound pressure, x_i is the Cartesian coordinate component, $f=0$ is the equation of the source surface, H(f) is the Heaviside function, ρ_0 is the density of undisturbed fluid, $\mathrm{v_n}$ is the component of the source surface velocity in outer normal direction, $p_{ij}=p\delta_{ij}-\sigma_{ij}$ is the fluid compressive stress tensor, where p is the pressure, σ_{ij} is the viscous stress, T_{ij} is the Lighthill stress tensor. For flow with high Reynolds number and low Mach number, $T_{ij}\approx\rho u_i u_j$, where u_i is the component of fluid velocity in the x_i direction.

According to Lighthill's acoustic analogy, the three terms on the right side in Eq. (3) represent monopole source, dipole source, and quadrupole source, respectively. The sound pressure $p'(\mathbf{x},\ t)$ at far-field measurement point $\mathbf{x}$ is the superposition of contributions of the three source terms:

$$p'(\mathbf{x},\ t)=p'_T(\mathbf{x},\ t)+p'_L(\mathbf{x},\ t)+p'_Q(\mathbf{x},\ t) \quad (4)$$

where $p'_T(\mathbf{x},\ t)$, $p'_L(\mathbf{x},\ t)$ and $p'_Q(\mathbf{x},\ t)$ are the sound pressures generated by monopole sources, dipole sources and quadrupole sources, respectively.

The time–space integral solutions of the far-field noise of the three source terms are given by Farassat and Brentner

[27, 28]. In current study, the numerical simulation is based on wind tunnel mode and the train is a static rigid surface. Under such conditions, the solutions given by Farassat et al. can be simplified and their expressions are

$$p'_T(\mathbf{x}, t) = 0 \tag{5}$$

$$p'_L(\mathbf{x}, t) = \frac{1}{4\pi}\int_{f=0}\left(\frac{\dot{l}_i\hat{r}_i}{c_0 r}+\frac{l_i\hat{r}_i}{r^2}\right)_{ret}\mathrm{d}S \tag{6}$$

$$p'_Q(\mathbf{x}, t) \tag{7}$$
$$= \frac{1}{4\pi}\int_{f>0}\left(\frac{\ddot{T}_{ij}\hat{r}_i\hat{r}_j}{c_0^2 r}+\frac{3\dot{T}_{ij}\hat{r}_i\hat{r}_j-\dot{T}_{ii}}{c_0 r^2}+\frac{3T_{ij}\hat{r}_i\hat{r}_j-T_{ii}}{r^3}\right)_{ret}\mathrm{d}V$$

In Eqs. (6 and 7), r is the distance between the sound source point and the receiver, $\hat{r}_i$ is the unit vector in the direction of the source point to the receiver. As the viscous stress σ_{ij} is small and can be ignored, $l_i \approx p\hat{n}_i$. The superscript "$\dot{T}$" represents the derivative to time, and the superscript "$\ddot{T}$" represents the second derivative to time. The symbol $f = 0$ under the integral sign indicates that the integration is carried out on the source surface and $f > 0$ indicates that the integration is carried out in fluid space outside the source surface. The subscript *ret* indicates that the variables in brackets are evaluated at emission time.

Under acoustic far-field condition, the sound pressures in Eqs. (6 and 7) are mainly determined by terms multiplied by factor r^{-1}, that is, the following approximations hold true [29, 30].

$$p'_L(\mathbf{x}, t) \approx \frac{1}{4\pi c_0}\int_{f=0}\left(\frac{\dot{p}n_i\hat{r}_i}{r}\right)_{ret}\mathrm{d}S \tag{8}$$

$$p'_Q(\mathbf{x}, t) \approx \frac{1}{4\pi c_0^2}\int_{f>0}\left(\frac{\ddot{T}_{ij}\hat{r}_i\hat{r}_j}{r}\right)_{ret}\mathrm{d}V \tag{9}$$

According to the integrated terms in Eqs. (8 and 9), the dipole source intensity at a point on the source surface mainly depends on the changing rate of pressure with time, and the quadrupole source intensity at a point in the fluid space depends on the second derivative of the Lighthill stress tensor with respect to time. Therefore, the root mean square value of the first derivative of pressure to time $(\partial p/\partial t)_{\mathrm{rms}}$ on the source surface can be used to characterize the dipole source intensity, and the root mean square value of the second derivative of the Lighthill stress tensor to time $(\partial^2 T_{ij}/\partial t^2)_{\mathrm{rms}}$ can be used to characterize the quadrupole source intensity.

3 CFD Model

3.1 Geometry Model, Computational Domain, and Boundary Conditions

A 1:8 scale electric multiple unit (EMU) model is taken as the research object, as shown in Fig. 1. The model consists of a head car, a mid car, and a tail car, equipped with six bogies. The considered bogie model preserves the essential geometric features of typical bogies and therefore is adequately representative. To simulate the underbody flow of the train more realistically, the track structures are also modeled. It should be noted that when using a scale model, the corresponding Reynolds number decreases. However, if the Reynolds number exceeds a critical value, the Reynolds number effect is generally negligible. Referring to some previous studies [10], it is expected that the results of current simulation are largely independent of Reynolds number.

The computational domain established for the train model is shown in Fig. 2. Taking the height of the train model (H = 474.5 mm) as characteristic length, the inlet boundary of the domain is $20H$ away from the train head, the outlet boundary is $45H$ away from the train tail, the height of the domain is $10.54H$, and the distances between both sides of the domain to the train are all $9.1H$. The boundary conditions of the computational domain are defined as follows: the inlet boundary is set as velocity inlet with inflow velocity of 97.22 m/s (350 km/h), the outlet boundary is set as pressure outlet with gauge pressure equal to 0. Both sides and top of the domain are set as symmetry boundaries. The ground and track surfaces are set as moving walls with the velocity same as inflow velocity to simulate the relative motion between the train and the ground during actual train operations.

3.2 Mesh Strategy

The hybrid mesh strategy of trimmed and prism layer mesh is used to discrete the computational domain. The maximum grid size of the head streamlined surface is 3 mm, the grid size of bogie cavity and bogie surface is controlled within 0.375 ~ 1.5 mm. 15 layers of fine prism layer grids with an initial height of 0.01 mm and a growth rate of 1.2 are generated on the train surface to accurately simulate the flow in the near wall region. The parameters of the prism layer mesh ensure an appropriate volume change of volume grids and make the wall y + values in most areas of the bogie surface less than two. Several blocks are established for local refinements of the volume mesh. The finest grid size of 1.5 mm is used for the bogie region. The total number of the volume grids is about 120 million. Figure 3 shows the meshing result.

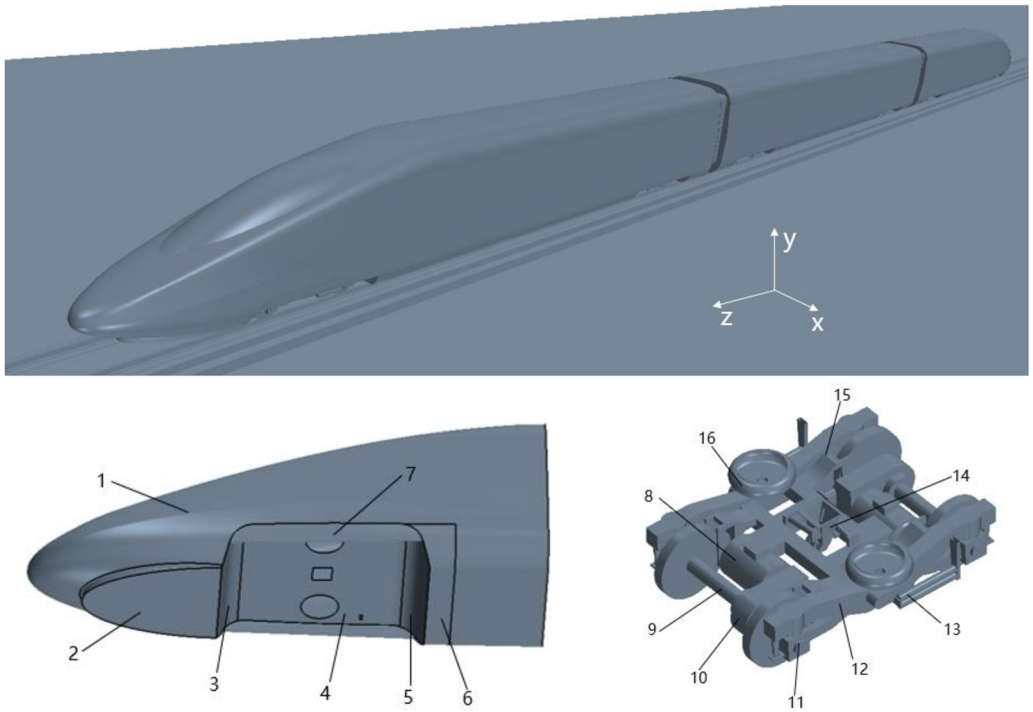

(1-Head streamlined surface; 2-Cowcatcher; 3-Front wall of bogie cavity; 4- Top wall of bogie cavity; 5- Rear wall of bogie cavity; 6-Carbody surface adjacent to bogie cavity; 7-Sideskirt; 8-Traction motor; 9-Wheelset; 10-Gear box; 11-Axle box; 12-Bogie frame; 13-Yaw damper; 14-Traction device; 15-Brake clamp; 16-Airspring)

Fig. 1 Geometry model

Fig. 2 Computational domain

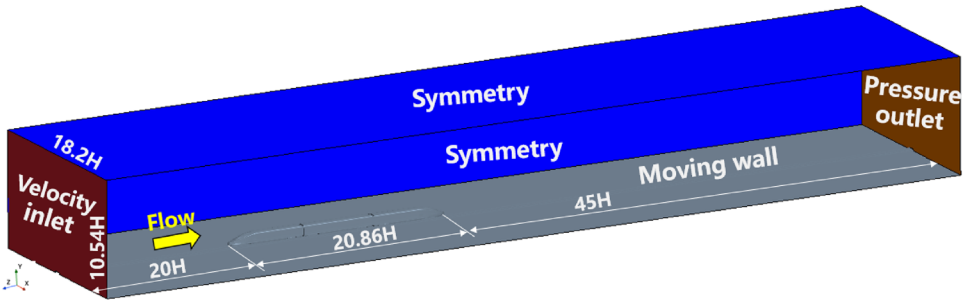

Fig. 3 Meshing result

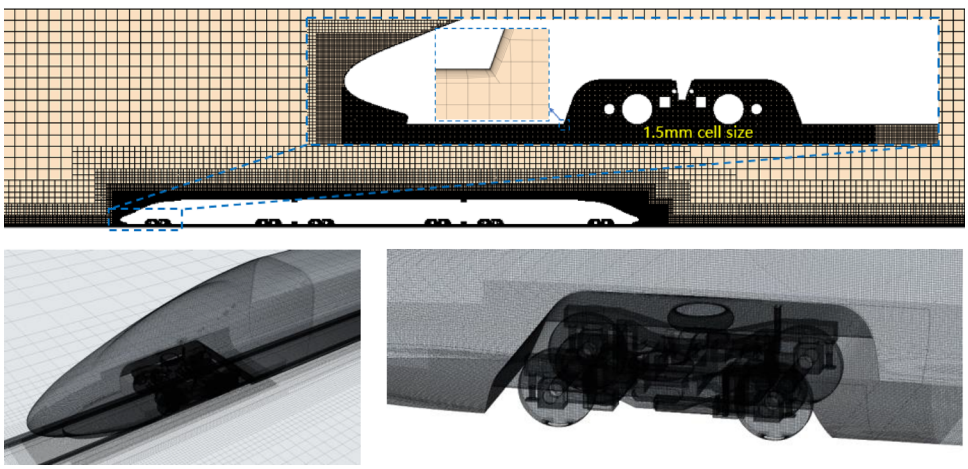

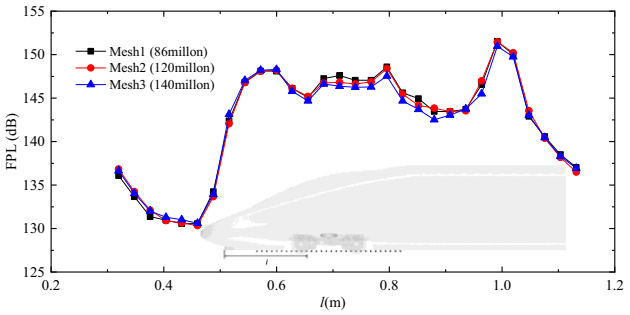

Fig. 4 Fluctuating pressure level beneath the bogie cavity

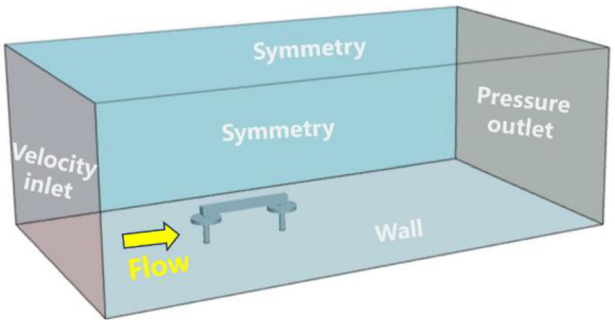

Fig. 5 The simple bogie model and its computational domain

3.3 Solver Setup

The flow field simulation and acoustic calculation are carried out in STAR-CCM + software. The Mach number of current simulation is less than 0.3, so air is considered as an incompressible gas [19, 20]. The segregated flow solver based on SIMPLE algorithm is used to solve the discretized flow governing equations. The second-order implicit method is adopted for time marching. To accelerate convergence, the transient simulation is initialized with a convergent steady flow field obtained by RANS simulation. The transient simulation is run for 0.3 s with a time step size of 1×10^{-4} s first, then the time step size is switched to 5×10^{-5} s and the simulation is run to 0.4 s. Finally, maintain the time step size of 5×10^{-5} s and run for another 0.25 s to calculate the far-field noise signal. The far-field noise is calculated by using the "Advanced time approach" proposed by Casalino [31], which allows calculating the noise signal, while solving the flow field with no need to store a large amount of flow field data in advance for acoustic post processing.

4 Validation of the Mesh Strategy and Numerical Methods

4.1 Mesh Independence Test

To assess the influence of grid size on simulation results, two additional sets of meshes are generated by adjusting the grid size in the bogie region. The resulting meshes consist of 86 million and 140 million volume cells, respectively. The fluctuating pressure level ($FPL = 20\log(p'_{\mathrm{rms}}/\, p_{\mathrm{ref}})$,$p'_{\mathrm{rms}}$ is the root mean square value of the fluctuating pressure, p_{ref} is reference pressure and is set as 2×10^{-5} Pa here) beneath the bogie cavity calculated by the three sets of meshes are compared, as shown in Fig. 4, where the abscissa l is the distance from a probe to the front end of the cowcatcher. For most of the probes, the difference among the results of the three sets of meshes is less than 1 dB. Therefore, the mesh parameters used in the current research is considered to meet the requirements for grid independence.

4.2 Simple Bogie Case Validation

The simple bogie case proposed by Zhu [16] is chosen to further validate the numerical methods in current study. The bogie model is composed of two wheelsets and two simple side frames, with the axle diameter equal to 17.5 mm and wheel diameter equal to 92 mm (1:10 scale). The wind tunnel test in [16] was conducted on a half-bogie model in an open-jet anechoic wind tunnel, with inflow velocity of 30 m/s. In the test, the half-bogie model was installed on a rigid baffle with acoustic treatment. More information about the wind tunnel test can be found in [16]. A CFD model that matches the configurations of the wind tunnel test is established, as shown in Fig. 5. The mesh for this case is generated based on the mesh parameters shown in Sect. 3.2, and the number of volume cells is about 3.9 million.

The far-field noise at the receiver named as top microphone in [16] is used to validate the numerical results. Figure 6 compares the spectrum results obtained by current simulation, Zhu's simulation and wind tunnel test. The simulation results have a frequency resolution of 6 Hz that is the same as the test result. As can be seen, for this benchmark case, the current simulation obtains similar result to that of Zhu's simulation. The spectrum result obtained by wind tunnel test is much smoother than that obtained by numerical simulation, this is because the test spectrum is obtained by averaging the spectrum results of multiple data segments. However, the numerical results and test result are in good agreement in terms of spectrum shape and dominant frequency. The peak frequency in the wind tunnel test results is 314 Hz and that predicted by current simulation is 318 Hz. The discrepancy in sound pressure level at the dominant frequency between the spectra of current simulation and wind tunnel test is about 2 dB. In general, these comparisons further validate the reliability of the mesh parameters and numerical methods in current research.

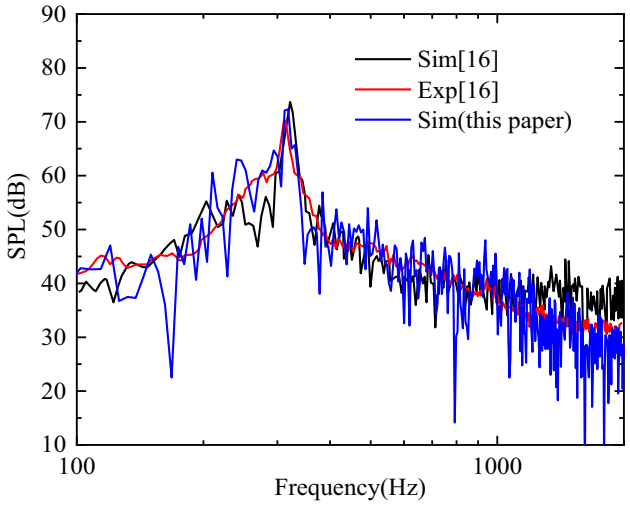

Fig. 6 Comparison of simulation and wind tunnel test results of the simple bogie model

5 Results and Discussions

The analysis of the simulation results is focused on the foremost bogie region of the head car. Firstly, the airflow path in the bogie region is analyzed to provide a basic understanding of the flow characteristics in the bogie region. Then, the distribution of dipole and quadrupole sources in the bogie region are presented and the formation mechanism of the noise sources are analyzed. Finally, the far-field noise characteristics of the bogie region are discussed.

5.1 Airflow Path in the Bogie Region

Figure 7 depicts the three-dimensional streamlines in the bogie region. The two clusters of streamlines are emitted from section S1 beneath the train and section S2 on the side of the train, respectively (shown in the upper left corner of Fig. 7), and they clearly illustrate the path of airflow entering and exiting the bogie cavity. It is evident that the airflow inside the bogie cavity mainly comes from the bottom of the train rather than both sides of the train. Beneath the train, the airflow traverses across the front section of the bogie cavity and then rolls up to enter the cavity from the gaps between the bogie frame, rear wheelset, and the cavity rear wall. After that, the airflow recirculates back toward the front of the bogie cavity slowly, part of the airflow exits the bogie cavity from the gaps between the cavity front wall, front wheelset and the bogie frame, merging into the high-speed airflow beneath the train. Simultaneously, the other part of the airflow exits from both sides of the cavity and merges into the high-speed airflow on both sides of the train.

5.2 Aerodynamic Noise Sources Identification of the Bogie Region

5.2.1 Dipole Sources in the Bogie Region

The time derivative of surface pressure is utilized to quantify the dipole source intensity. Figure 8 shows the distribution of the root mean square value of the pressure derivative to time $(\partial p/\partial t)_{\mathrm{rms}}$ in the bogie region. It is evident that the highest $(\partial p/\partial t)_{\mathrm{rms}}$ occurs at several specific locations, including the bottom surface of the cowcatcher, the lower sections of both windward and side surfaces of the wheels, the lower parts of the traction motors and gearboxes, the bottom surface of the bogie frame, the lower part of the bogie cavity rear wall and the carbody surface adjacent to the bogie cavity rear wall. Additionally, a relatively high $(\partial p/\partial t)_{\mathrm{rms}}$ distribution is observed on the outer surface of the yaw damper. Overall, these results are consistent with the noise source identification results reported in previous experimental studies [11–13].

The pressure fluctuations on solid surfaces typically arise from the interaction between vortex structures and the solid walls. To illustrate the formation mechanism of dipole sources in the bogie region in Fig. 8, Fig. 9 shows the instantaneous vorticity distribution on the mid-section of the computational domain and a horizontal section that passes through the yaw damper. By integrating this information with the streamline diagrams shown in Fig. 7, the motion path of the vortex structures convecting with the airflow in the bogie region, as well as their interactions with the components of the bogie region can be analyzed.

For the airflow beneath the train, it is evident from Figs. 7 and 9 that the airflow initially separates at the leading edge of the cowcatcher and the separated vortex structures impact the bottom surface of the cowcatcher. This interaction induces strong pressure fluctuations there, resulting in a crescent-shaped area with high $(\partial p/\partial t)_{\mathrm{rms}}$ distribution. Afterwards, the airflow reattaches to the bottom surface of the cowcatcher, flows downstream and separates again at the rear edge of the cowcatcher, leading to the formation of a shear layer. Due to the velocity gradient of the airflow inside and outside the bogie cavity, the shear layer exhibits Kelvin–Helmholtz instability. When the velocity differential surpasses a critical value, the shear layer loses stability and forms separated shear vortices. From Fig. 9, this occurs slightly anteriorly beneath the front axle. The separated shear vortex structures then convect downstream with the airflow beneath the train, roll up and invade into the cavity, leading to forceful impingements on the lower parts of both the bogie components and rear wall of the bogie cavity, which account for the high $(\partial p/\partial t)_{\mathrm{rms}}$ distributions at the bottom of the bogie (the lower parts of the wheels, traction motors and gearboxes, and the bottom surface of the bogie frame) and the rear wall of the bogie cavity

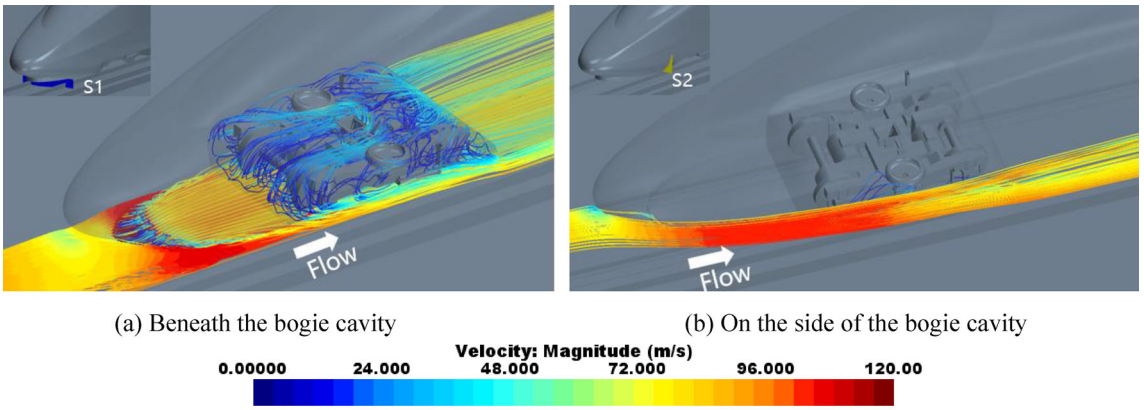

(a) Beneath the bogie cavity (b) On the side of the bogie cavity

Fig. 7 3-D streamline diagram in the bogie region

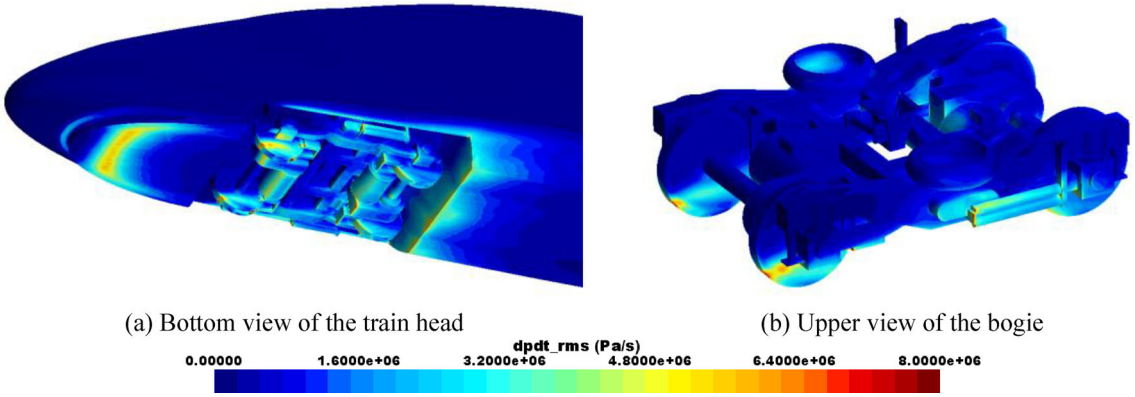

(a) Bottom view of the train head (b) Upper view of the bogie

Fig. 8 $(\partial p/\partial t)_{\mathrm{rms}}$ distribution in the bogie region

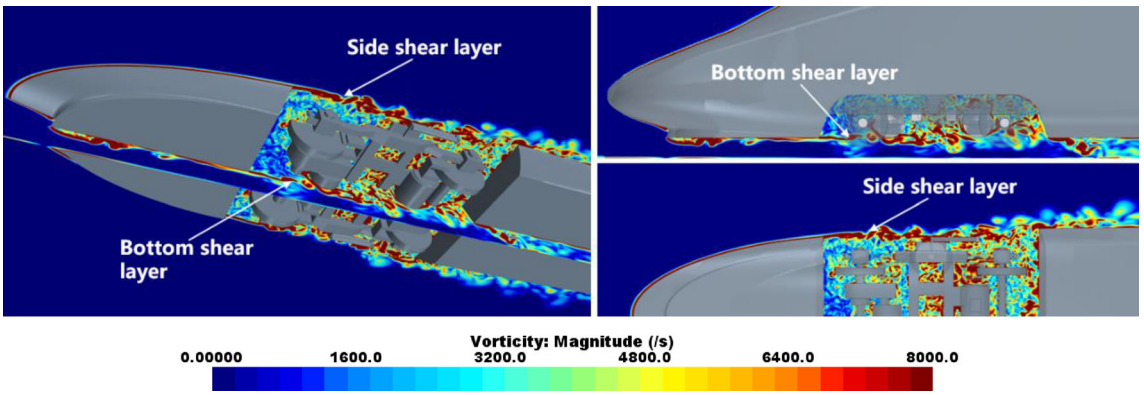

Fig. 9 Instantaneous vorticity distribution in the bogie region

shown in Fig. 8. Besides, after impacting the cavity rear wall, part of the broken vortex structures are thrown out of the cavity and interact with the carbody surface adjacent to the cavity rear wall, also resulting in strong pressure fluctuation there.

As shown in Fig. 9, the flow separations at the front side edges of the bogie cavity also lead to the formation of shear layers. According to the airflow path analysis, the side shear vortex structures will convect with the airflow on both sides of the cavity. Although the time-averaged streamline results in Fig. 7 show that the airflow almost never enters the bogie cavity from the side of the cavity, the instantaneous vorticity distribution in Fig. 9 indicates that the shear vortex structures formed at the front side edge of the bogie cavity will continuously grow and oscillate laterally when moving downstream, thus some vortex structures are still possible to invade into the cavity. Obviously, the high $(\partial p/\partial t)_{\mathrm{rms}}$ distribution on the yaw damper surface and both sides of the cavity rear wall are caused by the impact of the shear vortex structures formed

at the front side edges of the bogie cavity. Similar to the situation beneath the bogie cavity, part of the vortex structures break up after hitting the side corners of the cavity rear wall and continue to move downstream to interact with the adjacent carbody surface, also resulting in strong pressure fluctuation there.

5.2.2 Quadrupole Sources in the Bogie Region

The root mean square value of the second derivative of the Lighthill stress tensor to time $(\partial^2 T_{ij}/\partial t^2)_{\mathrm{rms}}$ is utilized to quantify the quadrupole source intensity at a point in fluid space. Since, the Lighthill stress tensor is a symmetric tensor, only six of its nine components are independent. Figure 10 shows the distribution of $(\partial^2 T_{ij}/\partial t^2)_{\mathrm{rms}}$ on two sections cross the bogie region. As can be seen, the quadrupole sources in the bogie region are concentrated in the shear layers formed at the rear edge of the cowcatcher and front side edges of the bogie cavity. Among all the components of the Lighthill stress tensor, the streamwise component has the highest value of second-order time derivative. Combined with the distribution of dipole sources in the bogie region shown in Fig. 8, it can be found that the surfaces with high dipole source intensity are close to the fluid areas with high quadrupole source intensity (immersed in the bottom and side shear layers). In fact, some scholars believe that the dipole sources are not real sources, and the sound field radiated by the dipole sources in acoustic analogy theory is actually an equivalent of the scattering effects of solid surfaces on quadrupole sources [32–35]. From this perspective, it is reasonable that there is a certain consistency between the distributions of dipole sources with high-intensity and quadrupole sources with high-intensity. Usually, the quadrupole sources close to solid walls can be scattered more effectively, resulting the formation of dipole sources with enhanced sound radiation abilities. As the distance between the quadrupole sources and the solid wall increases, the intensity of the scattering sound field decreases rapidly [33, 35]. In [33], Crighton provided a more detailed elaboration on this effect through several cases with analytical solutions. In a word, the quadrupole source distribution in Fig. 10 provides another explanation for the dipole source distribution in the bogie region in Fig. 8.

Figure 11 shows the instantaneous distribution of the second derivative of the Lighthill stress tensor to time in the bogie region (only the result of $\partial^2 T_{zz}/\partial t^2$ is given here, other components have similar results). Figure 11a visualizes the instantaneous quadrupole source distribution in three-dimensional space in the form of threshold (areas where the absolute value of $\partial^2 T_{zz}/\partial t^2$ is greater than 10^{11}), and Fig. 11b shows the instantaneous distribution of $\partial^2 T_{zz}/\partial t^2$ on two specific sections. The results both exhibit an alternating distribution of positive and negative values of $\partial^2 T_{zz}/\partial t^2$. In Fig. 11a, high-intensity quadrupole sources are located beneath and at both sides of the bogie cavity. In Fig. 11b, the instantaneous distribution of $\partial^2 T_{zz}/\partial t^2$ is consistent with the instantaneous vorticity distribution in the bogie region shown in Fig. 9, which indicates that the quadrupole sources are generated in the turbulent vortex structures and again emphasizes the importance of the shear vortex structures beneath and at both sides of the bogie cavity in aerodynamic noise generation of the bogie region. In general, since the quadrupole sources are distributed in fluid space and can be considered as the real sources, the identification of the quadrupole sources can help to determine the key flow structures related to aerodynamic noise generation more conveniently.

5.2.3 Correlation of Noise Sources

In addition to quantifying the intensity of dipole and quadrupole sources, it is also necessary to investigate the correlation of the noise sources [36–38]. The correlation of noise sources can be characterized by correlation scales, which can also be interpreted as the local vortex scale. A larger correlation scale means that fluctuations of physical quantities in a larger area near a point are correlated to the fluctuations of physical quantities at that point, corresponding to higher radiation efficiency. The measure of the correlation of two signals is correlation coefficient, which is defined as the covariance of the two signals normalized by the product of their respective standard deviations. For a point on a source surface (or in fluid space), the correlation coefficient distribution of this point can be obtained by performing correlation calculation with other points on the source surface (or in fluid space), and the correlation scale of this point can be further obtained from this. By performing the same operations on all points on the source surface (or in fluid space), the distribution of correlation scales on the whole source surface (or in fluid space) can be obtained. However, excessive computation makes this operation somewhat impractical [38]. According to the noise source identification results, thirteen representative reference points are selected at the main noise source locations in the bogie region, as shown in Fig. 12. Among them, M1–M9 are used to evaluate the correlation of dipole sources (the variable used for correlation calculation is $\partial p/\partial t$), and M10–M13 are used to evaluate the correlation of quadrupole sources (the variable used for correlation calculation is $\partial^2 T_{zz}/\partial t^2$).

Figure 13 shows the distribution of correlation coefficients of several typical reference points, in which the areas with correlation coefficients within the range of 0.5–1 are considered as the correlation areas [38]. As can be seen, with the exception of the M1 point located at the front of the cowcatcher bottom, all other reference points have correlation areas characterized by similar elliptical shapes. Notably, the correlation area of point M1 displays a significantly elongated length in the spanwise direction, indicating that the vortex structures formed by the separation at the front edge

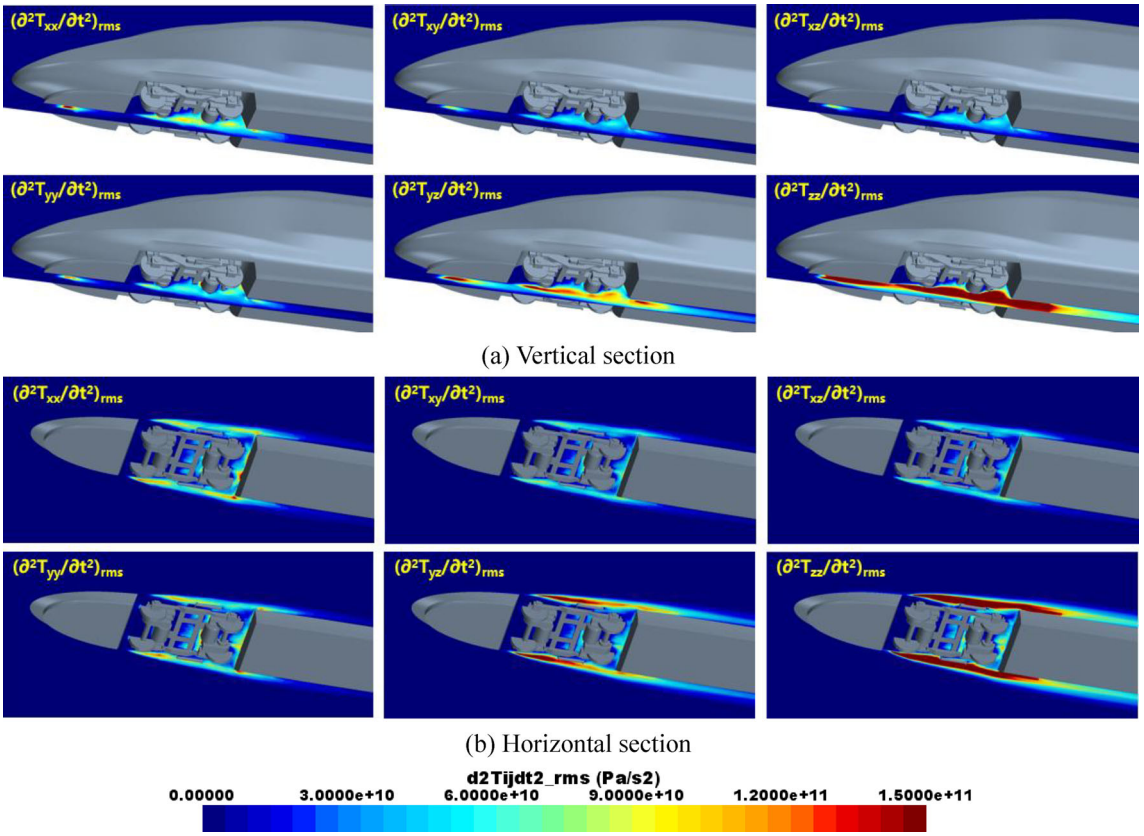

Fig. 10 $(\partial^2 T_{ij}/\partial t^2)_{\mathrm{rms}}$ distribution in the bogie region

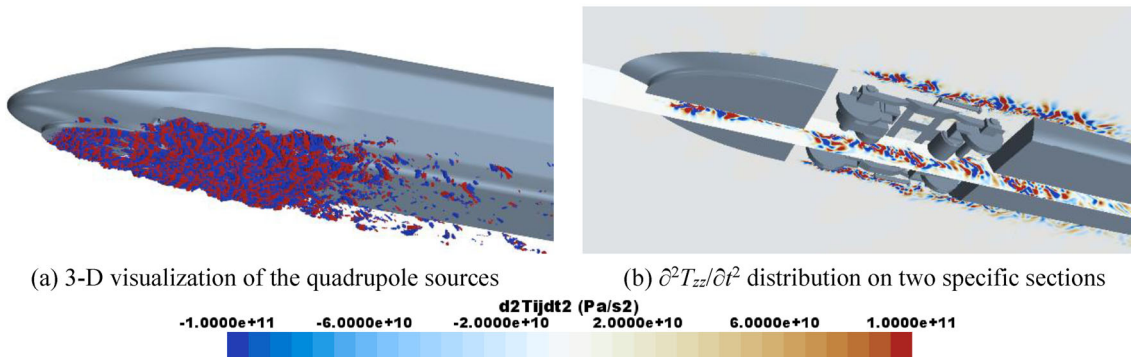

Fig. 11 Instantaneous distribution of $\partial^2 T_{zz}/\partial t^2$ in the bogie region

of the cowcatcher has stronger correlation in spanwise direction.

To estimate the correlation scales, the correlation areas of dipole and quadrupole sources are regarded as circles and spheres, respectively, and the corresponding radii are calculated as the correlation scales. Figure 14 summarizes the correlation scale results of each reference point. As can be seen, for dipole sources, the correlation scales of the points on the bogie surface exhibit relatively small differences and are slightly smaller than those of M1 on the bottom surface of the cowcatcher and M7 on the rear wall of the bogie cavity. For quadrupole sources, the correlation scale at M12 downstream the cavity is slightly larger, while the correlation scale at M13 in the side shear layer of the cavity is slightly smaller. In terms of the bogie region, the correlation scales of the points on (or near) the bogie cavity rear wall are larger than those on (or near) the bogie surface. This indicates that compared to the bogie, the vortex scales near the bogie cavity rear wall are larger, the flow field there tends to fluctuate at a lower frequency, and the aerodynamic noise sources there have a higher radiation efficiency. In addition, the correlation scales of dipole sources are significantly higher than those of

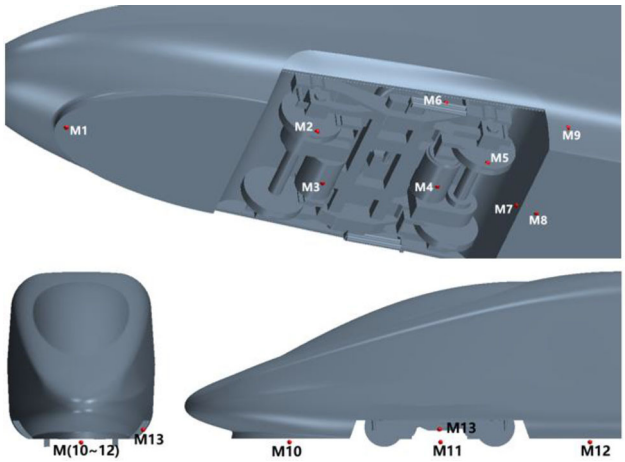

Fig. 12 Reference points for correlation calculation

quadrupole sources, indicating that the radiation efficiency of the dipole sources are significantly higher.

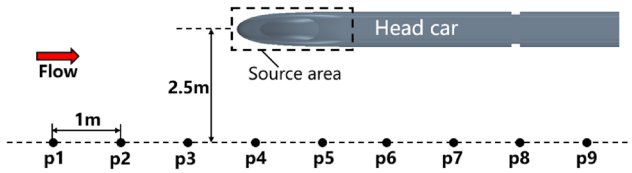

Fig. 15 Far-field noise measurement points at the trackside

5.3 Far-Field Noise Characteristics of the Bogie Region

5.3.1 Contribution Analysis

The arrangement of measurement points used for far-field noise assessment at the trackside is shown in Fig. 15, where the lateral distance from each point to the track centerline is 2.5 m and the longitudinal distance between the adjacent measuring points is 1 m. All the measurement points have the

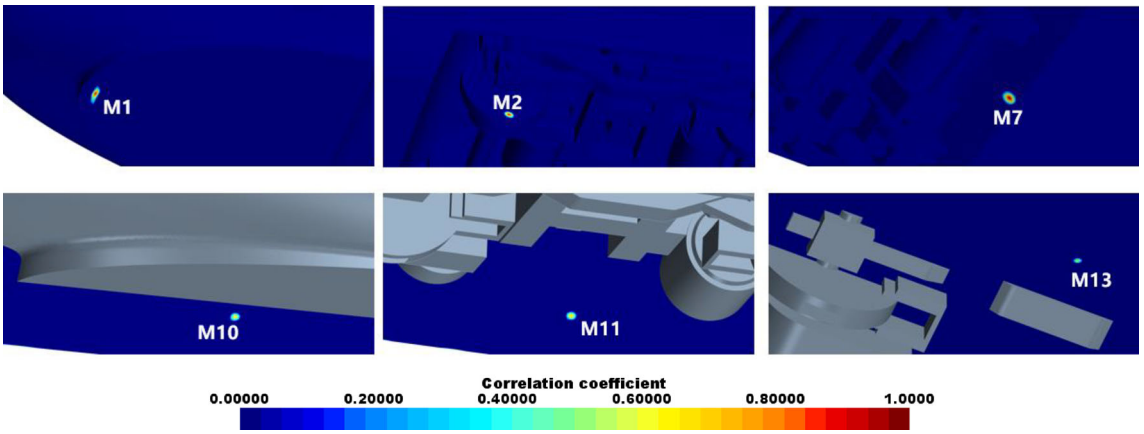

Fig. 13 Correlation areas of several reference points

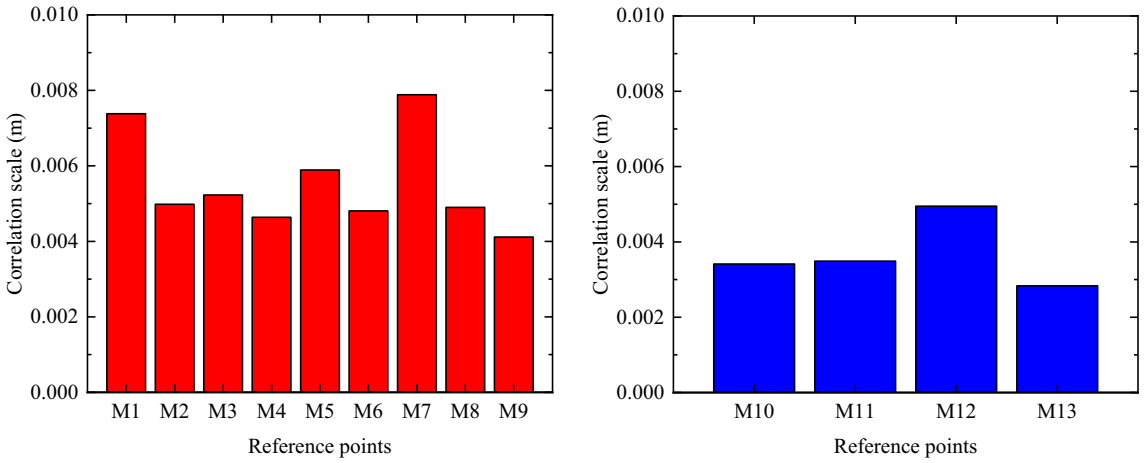

(a) Correlation scales of dipole sources

(b) Correlation scales of quadrupole sources

Fig. 14 Correlation scale results

same height from the ground as the bogie geometry center from the ground.

The contributions of the dipole and quadrupole sources to far-field noise are quantitatively compared first. According to the aerodynamic noise source identification results, the noise sources used for far-field noise calculation are defined. For dipole sources, the definitions of the source surfaces are shown in Table 1. For quadrupole sources, two volume source regions are defined, which are named as Q_V1 and Q_V2, as shown in Fig. 16. The Q_V1 mainly contains the contribution of quadrupole sources beneath the cowcatcher and around the bogie region, while the Q_V2 contains the quadrupole sources around the whole train head.

Figure 17a shows the comparison of the overall sound pressure level (OASPL) of the radiated noise of dipole and quadrupole sources at measurement points p1–p9. Wherein, the dipole noise is calculated by using two source surfaces, the train head and bogie region, and the quadrupole noise is calculated by using the volume source regions Q_V1 and Q_V2. It can be seen that the OASPL of dipole noise is much higher than that of quadrupole noise, with a difference of about 50 dB. Therefore, at a speed of 350 km/h, the aerodynamic noise of the bogie region is still dominated by dipole sources.

Figure 17b illustrates the OASPL results of dipole noise at p1–p9 when different components are employed as source surfaces. It is evident from Fig. 17b that the bogie is the most significant noise source for points p1–p9, followed by the bogie cavity. At p1, p2, p8, and p9, the contribution of the bogie cavity to far-field noise is equally important as that of the bogie itself, while at p5 that on the side of the bogie, the contribution of the bogie cavity to total noise is negligible. In contrast to the bogie cavity, there exists a relatively prominent influence of head streamlined surface on total noise at p5, while its significance can be disregarded for other measurement points. Furthermore, contributions from dipole sources on both the cowcatcher and the carbody surface adjacent to the bogie cavity rear wall to total noise at p1–p9 are also negligible.

Figure 18 shows the spectrum results of p2 and p5 with the train head, bogie region, bogie, and bogie cavity used as source surfaces. At p2, the spectrum results of the train head and bogie region exhibit a remarkable overlap above 200 Hz, indicating that the noise at p2 is almost completely contributed by the bogie region, and this is also consistent with the results in Fig. 17. Besides, comparing the spectrum results of the bogie itself and bogie cavity, it can be found that within the frequency band below 1000 Hz, the contributions of the bogie and bogie cavity are equally important, while for frequency band above 1000 Hz, the contribution of the bogie is higher than that of the bogie cavity. Considering, that some small components have been removed in the current bogie model, the real bogie model is expected to have a higher contribution to the noise within this frequency range. As the aerodynamic noise frequency is approximately in inverse proportional to model scale (assuming that the Strouhal number based on model scale is approximately a constant), this frequency boundary is about 125 Hz for a full-scale train model. At p5, the sound pressure level below 2000 Hz is higher when using the train head as source surface compared to employing the bogie region as source surface. According to the results in Fig. 17, this difference is due to the contribution of the dipole sources on the head streamlined surface.

It is worth noting that in the noise source identification results, high $(\partial p/\partial t)_{\mathrm{rms}}$ values also appear on the bottom surface of the cowcatcher and carbody surface adjacent to the bogie cavity rear wall, but the results in Fig. 17 suggest that they have minor contribution to the total noise at the track-side, which is related to the directivity of the sources and the areas of the source surfaces. On the head streamlined surface, the dipole source intensity ($(\partial p/\partial t)_{\mathrm{rms}}$) is low, but it can also produce significant noise contributions at specific positions, which is mainly due to its large sound source area. In addition, except for the bogie cavity, the changes in noise level of other source surfaces from p1 to p9 are basically consistent with the change of the distance between the measurement point and source surface. However, when the bogie cavity is used as source surface, the maximum OSAPL appears at p1 and p9, and that at p5 is the minimum, which can also be attributed to the directivity of the bogie cavity.

5.3.2 Directivity Analysis

Figure 19 shows the directivity curves of far-field noise of different source surfaces, which are drawn based on the OASPL results of the measurement points on a horizontal circle and a vertical circle with circle centers coinciding with the geometry center of the bogie and radii of 2.5 m. It should be noted that due to the usage of the incompressible gas model and the solid surface formula of the FW-H equation, the current simulation does not consider the shielding and scattering effects of the carbody and track structures. The directivity results of the bogie components shown in Fig. 19 are equivalent to the sound radiation characteristics of each component in free space.

In most directions, the far-field noise is dominated by the dipole sources in the bogie region. Only in a small range of radiation angle on both sides of the bogie, the dipole sources on the head streamlined surface have a relatively significant contribution. In XOY plane, the dipole noise generated by the bogie region mainly radiates upwards. On both sides of the bogie region, with the radiation angle ranging from 0° to 30° and 150° to 180°, the dipole noise is mainly contributed by the bogie itself. Above the bogie, with the radiation angle

Table 1 Definitions of dipole source surfaces

Source surface	Components included (Fig. 1)
Train head	1,2,3,4,5,6,7,8,9,10,11,12,13,14,15,16
Bogie region	3,4,5,6,7,8,9,10,11,12,13,14,15,16
Bogie	8,9,10,11,12,13,14,15,16
Bogie cavity	3,4,5
Carbody surface adjacent to bogie cavity	6
Cowcatcher	2
Head streamlined surface	1

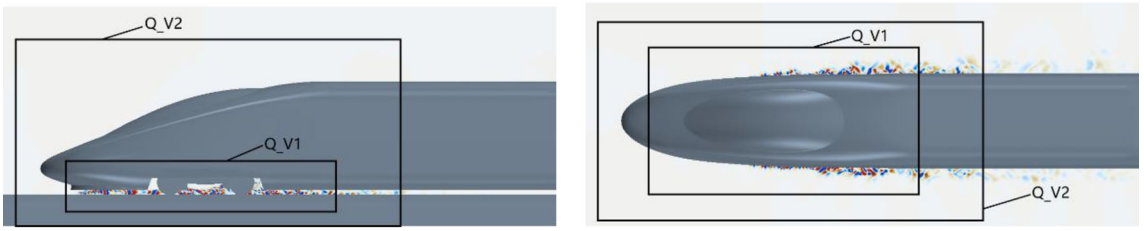

(a) Side view (b) Top view

Fig. 16 Definition of quadrupole noise source regions

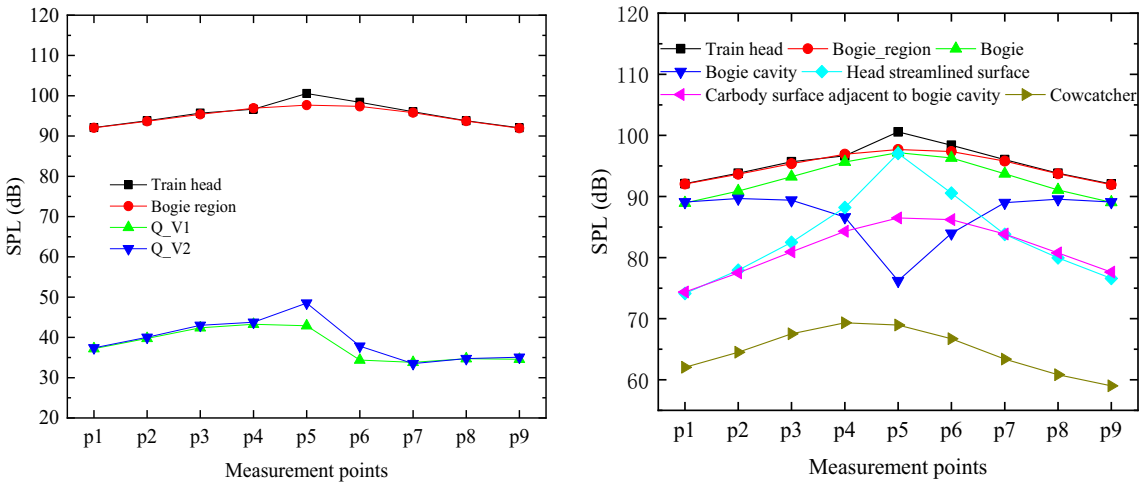

(a) Contribution of dipole and quadrupole sources (b) Contribution of bogie components

Fig. 17 Source contribution analysis

ranging from 60° to 120°, the dipole noise is mainly contributed by the bogie cavity. In addition, the dipole sources on the cowcatcher and the carbody surface adjacent to the bogie cavity also mainly radiate upwards and have little contribution to the noise at the bogie side. On the contrary, the dipole sources on the head streamlined surface mainly radiates to both sides. In XOZ plane, there exists a relatively uniform distribution of noise generated by the bogie region. The noise generated by the bogie itself also exhibits a uniform distribution in all directions, while the noise generated by the bogie cavity presents characteristics of a dipole source fluctuating in the inflow direction. On both sides of the bogie, the aerodynamic noise generated by the bogie region is mainly contributed by the bogie itself, while in front and rear directions of the bogie region, the contributions of the bogie and bogie cavity are equally important. Additionally, the head streamlined surface and carbody surface adjacent to bogie cavity both show characteristics of dipole sources fluctuating in lateral direction.

In Eq. (8), the term that determine the directivity of the source is $n_i \hat{r}_i$, which is the cosine value of the angle θ

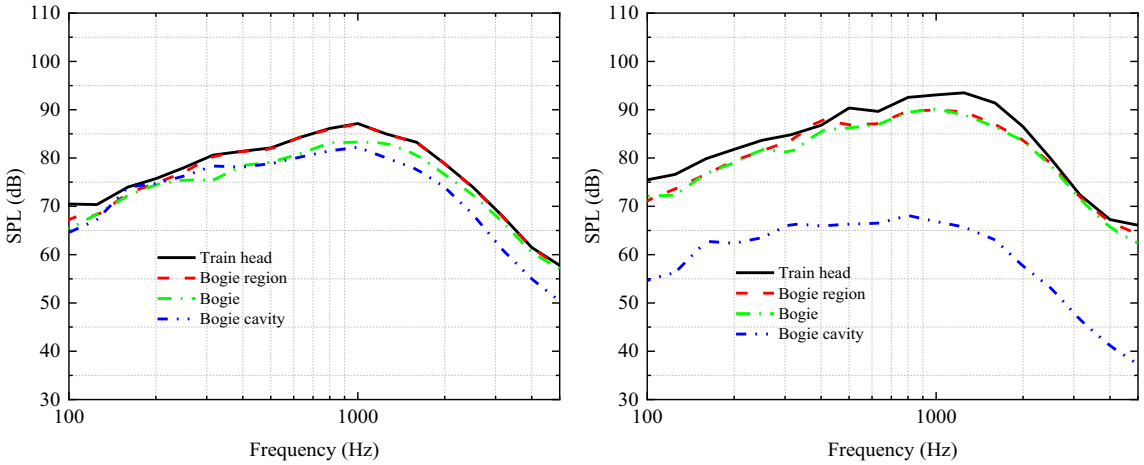

(a) p2 (b) p5

Fig. 18 Sound pressure level spectrum at p2 and p5 (1/3 octave band)

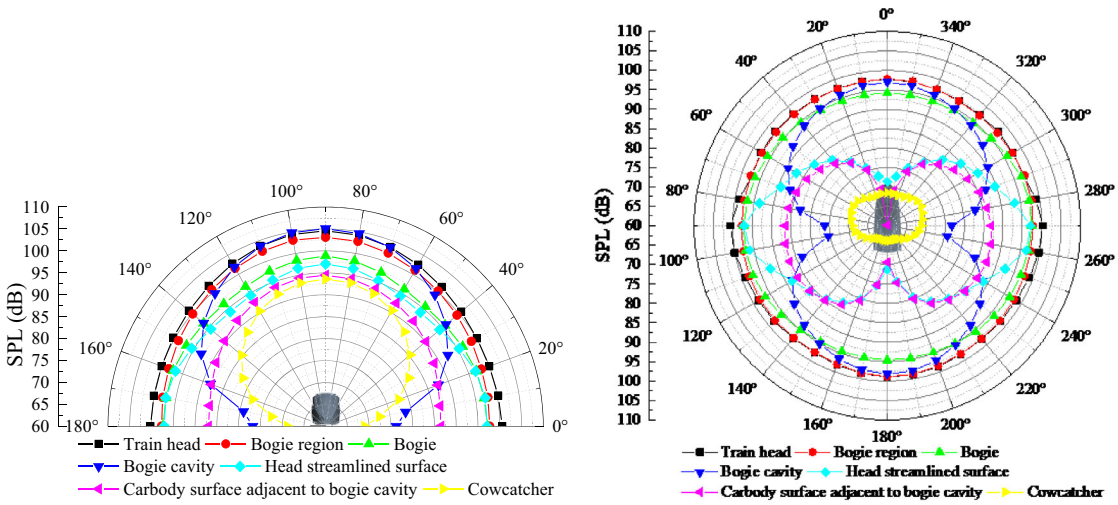

(a) XOY plane (b) XOZ plane

Fig. 19 Directivity results

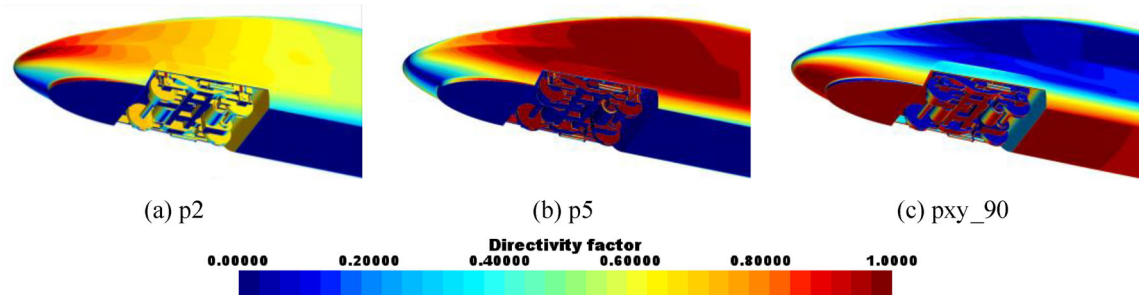

(a) p2 (b) p5 (c) pxy_90

Fig. 20 Visualization of directivity factors of dipole sources on the train surface

between the outer normal direction at a point on source surface and its orientation towards the receiver. To better understand the directivity of each component, the distribution of the absolute value of this directivity factor on the train surface for measurement points p2, p5 and pxy_90 (point at 90° in XOY plane, just above the bogie) are displayed to visualize the directivity of source surfaces, as shown in Fig. 20.

Combined with the dipole source distribution shown in Fig. 8, the far-field noise results in Figs. 17 and 19 can be explained. For the bogie cavity, high-intensity dipole sources are located on the cavity rear wall. The included angle between the outer normal direction at a point on the cavity rear wall surface and its orientation towards p5 is close to 90°, and the directivity factor is close to zero. Consequently, the contribution of the bogie cavity to the total noise there is negligible. Along the direction from p5 to p1, the included angle between the outer normal direction of a point on the cavity rear wall surface and its orientation towards the receiver (p1 ~ p5) gradually decreases and the directivity factor cosθ gradually increases. Consequently, the contribution of bogie cavity to the total noise at p2 is more obvious than that at p5. For the cowcatcher, high-intensity dipole sources are located in the front of its bottom surface. The included angle between the outer normal direction of a point on the cowcatcher's bottom surface and its orientation towards p2 or p5 is close to 90°, and the directivity factor is close to zero, while for pxy_90, the directivity factor is close to one. Therefore, the noise generated by the cowcatcher mainly radiates upwards. Although the pressure fluctuation on the head streamlined surface has not been separately analyzed, it can be inferred from the directivity factor distribution that its noise contribution at p5 mainly comes from the dipole sources on its side part.

6 Conclusions

Combining the DDES model and FW-H acoustic analogy theory, a numerical investigation is conducted to enhance the comprehension of the noise generation mechanism of the high-speed train bogie region and provide valuable guidance for subsequent research on bogie noise reduction. The main conclusions of this study are as follows:

(1) The dipole sources in the bogie region are mainly distributed on the surfaces of components immersed in the shear layers that formed at the trailing edge of the cowcatcher and the front side edges of the bogie cavity, including the lower parts of the wheels, traction motors and gearboxes, the bottom surface of the bogie frame, the rear wall of the bogie cavity and the outer surface of the yaw damper. From the perspective of vortex-solid interaction, the high-intensity dipole sources at these positions are induced by the impingement of the shear vortex structures.

(2) The quadrupole sources in the bogie region are mainly distributed in the shear layers formed at the trailing edge of the cowcatcher and front side edges of the bogie cavity, that is, the surfaces with high dipole source intensity are close to the fluid areas with high quadrupole source intensity. This provides another explanation for the distribution of dipole sources in the bogie region. Because the sound field radiated by the dipole sources in acoustic analogy can also be understood as an equivalent of the scattering effects of the solid walls on quadrupole sources. The quadrupole sources close to the solid walls can usually be more effectively scattered, leading to the formation of dipole sources with enhanced sound radiation ability.

(3) At a speed of 350 km/h, the far-field aerodynamic noise of the bogie region is still dominated by the dipole sources. Although there are obvious differences between the radiation characteristics of the bogie itself and bogie cavity, their contributions to the far-field noise of the bogie region are equally important in general. However, it should be noted that despite the minimal contribution of the quadrupole sources to the far-field noise, the identification of quadrupole sources can determine the key flow structures related to aerodynamic noise generation more conveniently.

(4) The guideline for aerodynamic noise control of the bogie region can be summarized as minimizing the interaction between the bottom and side shear vortex structures and the bogie components, as well as the bogie cavity rear wall, or in other words, making the solid components of the bogie region far away from the high-intensity quadrupole sources (the bottom and side shear layers).

Acknowledgements This work was supported by National Natural Science Foundation of China (12172308) and National Key Research and Development Program of China (2020YFA0710902).

Funding National Natural Science Foundation of China, 12172308, Jiye Zhang

Declarations

Conflict of interest The authors declare that they have no conflict of interests.

References

1. Thompson, D.J., Iglesias, E.L., Liu, X., Zhu, J.Y., Hu, Z.W.: Recent developments in the prediction and control of aerodynamic noise from high-speed trains. Int. J. Rail Transp. **3**(3), 119–150 (2015). https://doi.org/10.1080/23248378.2015.1052996

2. Kurita, T.: Development of external-noise reduction technologies for Shinkansen high-speed trains. J. Environ. Eng. **6**(4), 805–819 (2011). https://doi.org/10.1299/jee.6.805
3. Zhang, J., Li, J.J., Tian, H.Q., Gao, G.J., Sheridan, J.: Impact of ground and wheel boundary conditions on numerical simulation of the high-speed train aerodynamic performance. J. Fluids Struct. **61**, 249–261 (2016). https://doi.org/10.1016/j.jfluidstructs.2015.10.006
4. Zhu, J., Hu, Z., Thompson, D.J.: The flow and flow-induced noise behaviour of a simplified high-speed train bogie in the cavity with and without a fairing. Proc. Inst. Mech. Eng., Part F: J. Rail Rapid Transit. **232**(3), 759–773 (2018). https://doi.org/10.1177/0954409717691619
5. Li, Z.M., Li, Q.L., Yang, Z.G.: Flow structure and far-field noise of high-speed train under ballast track. J. Wind Eng. Ind. Aerodyn. **220**, 104858 (2022). https://doi.org/10.1016/j.jweia.2021.104858
6. Zhu, J., Cheng, G., Li, Q., Chen, Y., Jia, Q.: Effect of bogie fairing on aerodynamic and aeroacoustic behaviour of a high-speed train nose car. Int. J. Rail Transp. **2023**, 1–17 (2023). https://doi.org/10.1080/23248378.2023.2250784
7. He, B., Xiao, X.B., Zhou, Q., Li, Z.H., Jin, X.S.: Investigation into external noise of a high-speed train at different speeds. J. Zhejiang Univ., Sci., A **15**(12), 1019–1033 (2014). https://doi.org/10.1631/jzus.A1400307
8. Yamazaki, N., Kitagawa, T., Uda, T., Nagakura, K., Iwasaki, M., et al.: Evaluation method for aerodynamic noise generated from the lower part of cars in consideration of the characteristics of underfloor flows on Shinkansen trains. Q. Rep. RTRI **57**(1), 61–68 (2016). https://doi.org/10.2219/rtriqr.57.1_61
9. Lauterbach, A., Ehrenfried, K., Loose, S., Wagner, S.: Microphone array wind tunnel measurements of Reynolds number effects in high-speed train aeroacoustics. Int. J. Aeroacoust. **11**(3–4), 411–446 (2012). https://doi.org/10.1260/1475-472X.11.3-4.411
10. Hao, N.S.: Research on high speed train aerodynamic noise wind tunnel test technology. Summary of the 2016 National Symposium on Aeroacoustics, (2016). (in Chinese)
11. Iglesias, E.L., Thompson, D.J., Smith, M., Kitagawa, T., Yamazaki, N.: Anechoic wind tunnel tests on high-speed train bogie aerodynamic noise. Int. J. Rail Transp. **5**(2), 87–109 (2017). https://doi.org/10.1080/23248378.2016.1274685
12. Yamazaki, N., Uda, T., Kitagawa, T., Wakabayashi, Y.: Influence of bogie components on aerodynamic bogie noise generated from Shinkansen trains. Q. Rep. RTRI **60**(3), 202–207 (2019). https://doi.org/10.2219/rtriqr.60.3_202
13. Sawamura, Y., Uda, T., Kitagawa, T., Yokoyama, H., Iida, A.: Measurement and reduction of the aerodynamic Bogie noise generated by high-speed trains in terms of wind tunnel testing. noise and vibration mitigation for rail transportation systems: Proceedings of the 13th International workshop on railway noise, (2019). https://doi.org/10.1007/978-3-030-70289-2_5
14. Meskine, M., Perot, F., Kim, M.S., Freed, D.M., Senthooran, S. et al.: Community noise prediction of digital high speed train using LBM. 19th AIAA/CEAS Aeroacoustics Conference, (2013). https://doi.org/10.2514/6.2013-2015
15. Sun, Z., Guo, D., Yao, S., Yang, G., Li, M.: Identification and suppression of noise sources around high speed trains. Eng. Appl. Comput. Fluid Mech. **7**(1), 131–143 (2013). https://doi.org/10.1080/19942060.2013.11015459
16. Zhu, J.: Aerodynamic noise of high-speed train bogies. University of Southampton, Southampton (2015)
17. Zhu, J., Hu, Z., Thompson, D.J.: Flow behaviour and aeroacoustic characteristics of a simplified high-speed train bogie. Proc. Inst. Mech. Eng., Part F: J. Rail Rapid Transit. **230**(7), 1642–1658 (2016). https://doi.org/10.1177/0954409715605129
18. Minelli, G., Yao, H.D., Andersson, N., Höstmad, P., Forssén, J., et al.: An aeroacoustic study of the flow surrounding the front of a simplified ICE3 high-speed train model. Appl. Acoust. **160**, 107125 (2020). https://doi.org/10.1016/j.apacoust.2019.107125
19. Li, Q.L., Li, Z.M., Yang, Z.G.: Noise contribution and coherence analysis of high-speed train head shape under moving slab track. Proc. Inst. Mech. Eng., Part F: J. Rail Rapid Transit. **237**(7), 848–857 (2023). https://doi.org/10.1177/09544097221140200
20. He, Y., Thompson, D.J., Hu, Z.: Aerodynamic noise from a high-speed train bogie with complex geometry under a leading car. J. Wind Eng. Ind. Aerodyn. **244**, 105617 (2024). https://doi.org/10.1016/j.jweia.2023.105617
21. Menter, F.R., Kuntz, M.: Adaptation of Eddy-Viscosity turbulence models to unsteady separated flow behind vehicles. The aerodynamics of heavy vehicles: trucks, buses, and trains. Lect. Notes Appl. Comput. Mech. (2004). https://doi.org/10.1007/978-3-540-44419-0_30
22. Shur, M.L., Spalart, P.R., Strelets, M.K., Travin, A.K.: A hybrid RANS-LES approach with delayed-DES and wall-modelled LES capabilities. Int. J. Heat Fluid Flow **29**(6), 1638–1649 (2008). https://doi.org/10.1016/j.ijheatfluidflow.2008.07.001
23. Shi, J.W., Zhang, J.Y.: Effect of Bogie Cavity End Wall Inclination on Flow Field and Aerodynamic Noise in the Bogie Region of High-Speed Trains. CMES-Comput. Model. Eng. Sci. **139**(2), 2175–2195 (2024). https://doi.org/10.32604/cmes.2023.043539
24. Shi, J.W., He, Y., Zhang, J.Y., Li, T.: Effect of geometry simplification and boundary condition specification on flow field and aerodynamic noise in the train head and bogie region of high-speed trains. J. Zhejiang Univ.-SCI. A (in press) (2023). https://doi.org/10.1631/jzus.A2300307
25. Siemens PLM Sofware. STAR-CCM+ User Guide (Version 12.04), (2017)
26. Williams, J.F., Hawkings, D.L.: Sound generation by turbulence and surfaces in arbitrary motion. Philos. Trans. R. Soc. Lond. Series A **264**(1151), 321–342 (1969). https://doi.org/10.1098/rsta.1969.0031
27. Farassat, F.: Linear acoustic formulas for calculation of rotating blade noise. AIAA J. **19**(9), 1122–1130 (1981). https://doi.org/10.2514/3.60051
28. Brentner, K.S.: An efficient and robust method for predicting helicopter high-speed impulsive noise. J. Sound Vib. **203**(1), 87–100 (1997). https://doi.org/10.1006/jsvi.1996.0834
29. Curle, N.: The influence of solid boundaries upon aerodynamic sound. Proc. R. Soc. A **231**(1187), 505 (1955). https://doi.org/10.1098/rspa.1955.0191
30. Bastin, F., Lafon, P., Candel, S.: Computation of jet mixing noise due to coherent structures: the plane jet case. J. Fluid Mech. **335**, 261–304 (1997). https://doi.org/10.1017/S0022112096004582
31. Casalino, D.: An advanced time approach for acoustic analogy predictions. J. Sound Vib. **261**(4), 583–612 (2003). https://doi.org/10.1016/S0022-460X(02)00986-0
32. Powell, A.: Aerodynamic noise and the plane boundary. J. Acoust. Soc. Am. **32**(8), 982–990 (1960). https://doi.org/10.1121/1.1908347
33. Crighton, D.G.: Basic principles of aerodynamic noise generation. Prog. Aerosp. Sci. **16**(1), 31–96 (1975). https://doi.org/10.1016/0376-0421(75)90010-X
34. Bailly, C., Bogey, C., Gloerfelt, X.: Some useful hybrid approaches for predicting aerodynamic noise. Comptes Rendus Mécanique **333**(9), 666–675 (2005). https://doi.org/10.1016/j.crme.2005.07.006
35. Gloerfelt, X., Pérot, F., Bailly, C., Juvé, D.: Flow-induced cylinder noise formulated as a diffraction problem for low Mach numbers. J. Sound Vib. **287**(1–2), 129–151 (2005). https://doi.org/10.1016/j.jsv.2004.10.047
36. King, W.F., III.: On the role of aerodynamically generated sound in determining wayside noise levels from high speed trains. J.

Sound Vib. **54**(3), 361–378 (1997). https://doi.org/10.1016/0022-460X(77)90445-X
37. Kim, S.E., Dai, Y., Koutsavdis, E., Sovani, S., Kadam, S., Ravuri, K.A.: versatile implementation of acoustic analogy based noise prediction method in a general-purpose CFD code. 9th AIAA/CEAS Aeroacoustics Conference and Exhibit, (2003). https://doi.org/10.2514/6.2003-3202
38. Phan, V.L., Tanaka, H., Nagatani, T., Wakamatsu, M., Yasuki, T.: A CFD analysis method for prediction of vehicle exterior wind noise. SAE Int. J. Passeng. Cars-Mech. Syst. **10**(1), 286–299 (2017). https://doi.org/10.4271/2017-01-1539